JACS Au
AN OPEN ACCESS JOURNAL OF THE AMERICAN CHEMICAL SOCIETY

Structural Basis for Inhibition of Urate Reabsorption in URAT1

Junping Fan,*,‡ Wenjun Xie,‡ Han Ke,‡ Jing Zhang, Jin Wang, Haijun Wang, Nianxin Guo, Yingjie Bai, and Xiaoguang Lei*

Cite This: *JACS Au* 2025, 5, 1308−1319

ABSTRACT: The urate transporter 1 (URAT1) is the primary urate transporter in the kidney responsible for urate reabsorption and, therefore, is crucial for urate homeostasis. Hyperuricemia causes the common human disease gout and other pathological consequences. Inhibition of urate reabsorption through URAT1 has been shown as a promising strategy in alleviating hyperuricemia, and clinical and preclinical drug candidates targeting URAT1 are emerging. However, how small molecules inhibit URAT1 remains undefined, and the lack of accurate URAT1 complex structures hinders the development of better therapeutics. Here, we present cryoelectron microscopy structures of a humanized rat URAT1 bound with benzbromarone, lingdolinurad, and verinurad, elucidating the structural basis for drug recognition and inhibition. The three small molecules reside in the URAT1 central cavity with different binding modes, locking URAT1 in an inward-facing conformation. This study provides mechanistic insights into the drug modulation of URAT1 and sheds light on the rational design of potential URAT1-specific therapeutics for treating hyperuricemia.

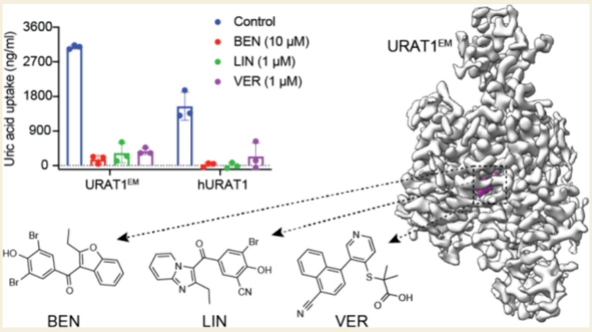

KEYWORDS: *URAT1, uric acid, hyperuricemia, drug discovery, cryo-EM structure*

INTRODUCTION

Uric acid (UA), mainly existing as the deprotonated form of urate under physiological conditions, is the end metabolite of purines produced by xanthine oxidase.[1] Humans and many other primates have 3−10-fold higher serum uric acid (SUA) levels than other mammals owing to loss-of-function mutations in the uric acid oxidase,[2] which breaks down urate into 5-hydroxyisourate. Uric acid arguably has a role in immune response as an antioxidant[3] and may be a driving force for exchanging other critical anions.[4] However, elevated SUA levels (also known as hyperuricemia) affect ∼20% of the global population and cause gout with a high prevalence of 1−6.8% worldwide and other pathological consequences, including renal diseases, nephrolithiasis, hypertension, and vascular disease.[5] SUA levels are balanced between UA biogenesis and excretion, of which UA is extruded in the kidney (70%) and the gastrointestinal tract. Extensive studies have identified that multiple transporters are involved in the complicated processes of absorption and excretion of urate in the kidney,[4,6−10] among which URAT1 (encoded by *SLC22A12*) is the predominant transporter responsible for urate reabsorption.[11,12] URAT1 is abundantly expressed in the apical brush border membrane of the kidney, where it moves urate into the kidney cells by exchanging intracellular organic anions.[11] Drugs that inhibit the xanthine oxidase and UA reabsorption-related transporters, which decrease UA generation and increase UA excretion, respectively, have been clinically used in managing hyperuricemia-associated diseases.[13] Currently, clinically used nonselective inhibitors of UA transporters (known as uricosurics) include probenecid, benzbromarone, sulfinpyrazone, and lesinurad.[13,14] Recently, the potent URAT1 inhibitor dotinurad has been approved for treating gout in Japan,[15,16] the URAT1-specific verinurad has been evaluated by two phase II trials,[17,18] and many other inhibitors of URAT1 are undergoing various preclinical studies and clinical trials,[19−21] highlighting the importance of URAT1 in the treatment of hyperuricemia. URAT1 belongs to the solute carrier 22 (SLC22) family, members of which include organic anion transporters (OATs) and organic cation transporters (OCTs) and have key roles in the absorption and/or excretion of diverse endogenous metabolites and drugs and xenobiotic deposition.[22] Recent structural advances[23−30] have elucidated that SLC22 transporters assume a conserved major facilitator superfamily (MFS) fold and employ the alternating access transport mechanism.[31,32] He et al. reported the cryo-EM structures of URAT1(R477S) and URAT1(R477S) in complex with urate, albeit the URAT1(R477S) exhibits reduced transport activity. He et al. were also unable

Received: December 5, 2024
Revised: February 11, 2025
Accepted: February 12, 2025
Published: February 23, 2025

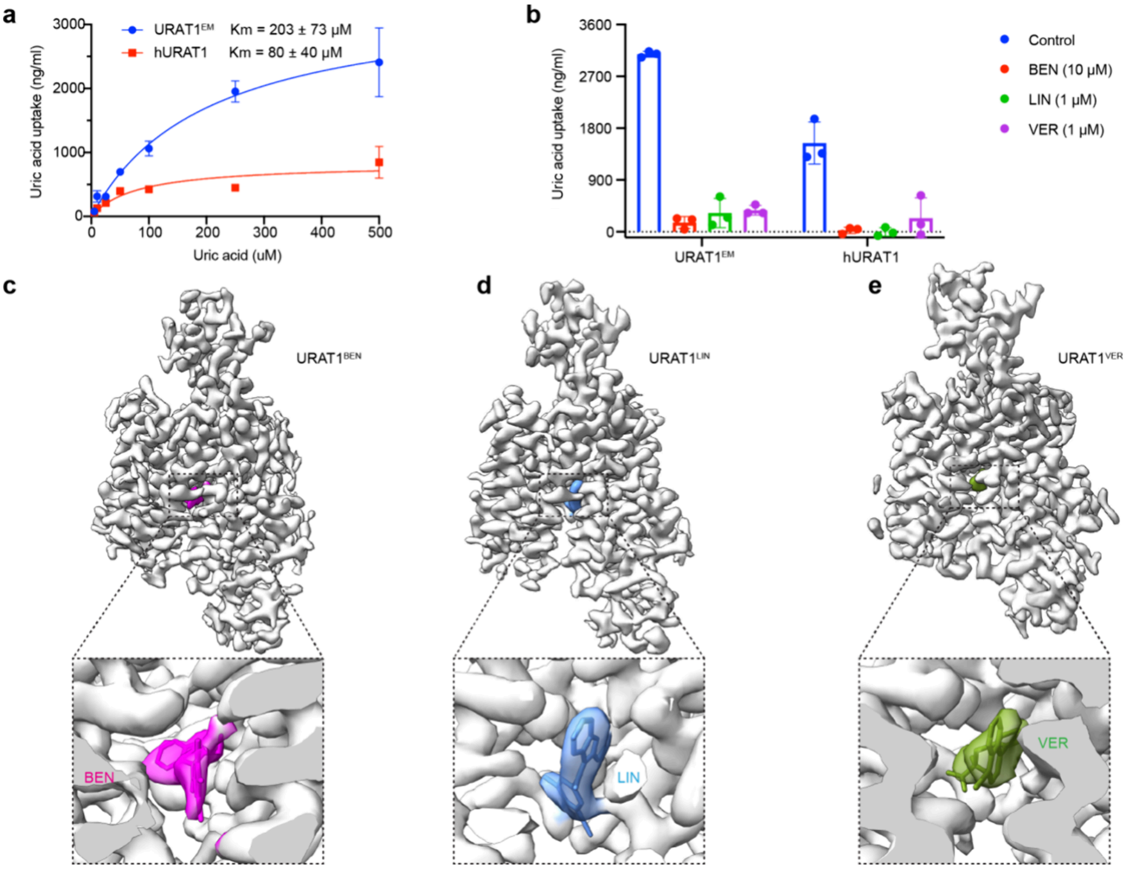

Figure 1. Functional characterization and EM structure of URAT1. (a) Concentration-dependent urate uptake by human wild-type (WT) and EM forms of URAT1. HEK293T cells were subjected to various concentrations of urate for 20 min. Cells expressing GFP served as controls. The basal uptake levels of GFP-expressing cells were subtracted. Data are presented as mean ± s.e.m.; $n = 3$ independent replicates. (b) Inhibition of urate uptake of WT and EM forms of URAT1 by benzbromarone, lingdolinurad, and verinurad. Cells were subjected to 250 μM urate with or without inhibitors. The basal uptake levels of GFP-expressing cells were subtracted. Data are presented as mean ± s.e.m.; $n = 3$ independent replicates. (c−e) EM density maps of URAT1 in complex with benzbromarone (c), lingdolinurad (d), and verinurad (e). Protein, benzbromarone, lingdolinurad, and verinurad are colored in white, purple, blue, and green, respectively.

to determine the structure of URAT1 in complex with its clinical drugs.[33] Dai and Lee reported cryo-EM structures of a chimeric human URAT1 in complex with urate and antigout drugs.[34] Most recently, three more nonpeer-reviewed URAT1 papers were posted on bioRxiv. Suo et al. determined URAT1 in complex with three clinically relevant inhibitors: benzbromarone, lesinurad, and compound TD-3.[35] Guo et al. reported the structures of URAT1 in complex with substrate urate or inhibitors benzbromarone and verinurad.[36] Wu et al. reported the structures of URAT1 bound with uric acid, dotinurad, benzbromarone, lesinurad, and verinurad.[37] However, considering the importance of URAT1 as a drug target, the structure of URAT1 and the precise binding modes of different small-molecule inhibitors in URAT1 remain to be explored. In this work, we carried out structural, functional, and computational analyses to elucidate the molecular mechanisms for urate transport and uricosuric inhibition of URAT1, providing critical structural insights into URAT1 pharmacology. Additionally, our URAT1 structures reveal detailed structure differences between URAT1 and OCT/OATs, which could serve as reliable templates for developing URAT1-specific therapeutics.

■ RESULTS AND DISCUSSION

Function and Structure of URAT1

We overexpressed human wild-type URAT1 (hURAT1) fused with a C-terminal GFP in HEK293T cells and probed its uric acid uptake activity using quantitative mass spectrometry analysis, which yielded a Michaelis−Menten constant (K_m) for urate in hURAT1 at 80 μM (Figure 1a), in agreement with the findings of a previous study.[38] However, purified samples of hURAT1 in detergents from HEK293T cells are heterogeneous and are not applicable for structural analysis (Figure S1a). To overcome this obstacle, we screened URAT1 from different species and found that rat URAT1 (rURAT1) exhibits improved stability and homogeneity (Figure S1b). Although rURAT1 shares a high sequence identity of ∼74% with hURAT1 and could accumulate uric acid to a lesser extent, it exhibits decreased affinity to uric acid and most hURAT1 inhibitors.[39,40] Substituting N35, Y365, and M481 of rURAT1 with S35, F365, and I481 from hURAT1 almost fully restored high affinity inhibition;[40] we, therefore, generated a humanized rURAT1 chimera with these three mutations of N35S, Y365F, and M481I (designated as rURAT1−3M), which exhibits a sharp and symmetric monodisperse peak from the size-exclusion chromatography (SEC) profile (Figure S1c). To facilitate cryo-EM structure determination, we moved GFP

https://doi.org/10.1021/jacsau.4c01188
JACS Au 2025, 5, 1308−1319

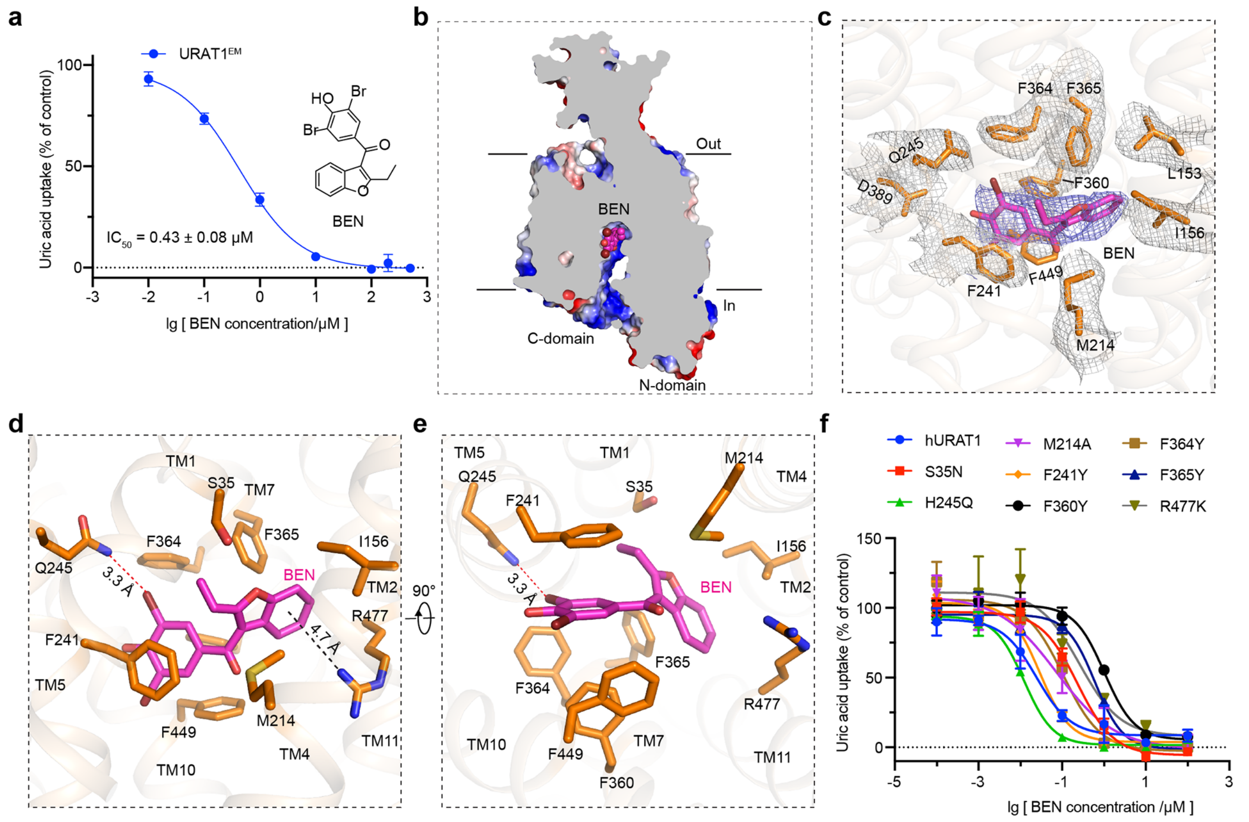

g

	hURAT1	S35N	H245Q	M214A	F241Y	F360Y	F364Y	F365Y	R477K
IC_{50} (μM)	0.024 ±0.010	0.234 ±0.058	0.012 ±0.002	0.075 ±0.058	0.029 ±0.006	1.025 ±0.185	0.107 ±0.033	0.608 ±0.128	0.264 ±0.179
Fold (/hURAT1)		10	0.5	3	1.2	43	4.5	25	11

Figure 2. Benzbromarone binding site in URAT1. (a) Concentration-dependent inhibition of URAT1^{EM} by benzbromarone. Data are normalized and presented as mean ± s.e.m.; *n* = 3 independent replicates. The chemical structure of benzbromarone is presented. (b) Cut-open electrostatic potential surface of URAT1^{BEN}. Positive and negative potentials are colored in blue and red, respectively. Benzbromarone is depicted in purple sticks. (c) EM density map for benzbromarone. The densities for benzbromarone and surrounding residues are shown in a blue and gray mesh, respectively. (d, e) Detailed benzbromarone site in URAT1. The side chains of residues involved in benzbromarone binding are shown as sticks. Red dashed lines indicate potential hydrogen bond interactions. (f, g) Inhibition of human URAT1 WT and variants by benzbromarone. Cells were incubated with either an assay buffer or a gradient of benzbromarone for 5 min before being exposed to 250 μM urate for 15 min. The basal uptake levels of GFP-expressing cells were subtracted. Data are normalized to their respective activities without benzbromarone and presented as mean ± s.e.m.; *n* = 3 independent replicates.

to the N-terminus and introduced a GFP-specific antibody to the C-terminus of rURAT1−3M, functioning as a fiducial marker for accurate particle alignments.[41,42] The resulting construct, namely, URAT1^{EM}, exhibits increased activity compared to hURAT1 and slightly decreased urate affinity, reflected by its K_m value of 203 μM, which is ∼2.5-fold of that in hURAT1 (Figure 1a). Additionally, the transport activity of URAT1^{EM} was efficiently inhibited by three clinically evaluated small-molecule inhibitors, benzbromarone (BEN), lingdolinurad (LIN, also known as ABP-671), and verinurad (VER), respectively (Figure 1b).

Next, we purified the URAT1^{EM} samples in the presence of those small-molecule inhibitors and analyzed them using cryo-EM single-particle analysis (Figures S1d−f and S2−S4). After extensive data processing, the final EM maps of URAT1^{EM} were gained at resolutions of 3.2−3.5 Å (Figures S2−S4 and Table S1). The models of URAT1^{EM} containing Met1 to Leu515 were achieved based on the EM maps with the assistance of the rURAT1 AlphaFold2 model.[43] Importantly, in the central cavities of the maps, we observed strong EM densities in distinct shapes, which facilitate the assignment of the small-molecule inhibitors of BEN, LIN, and VER (Figure 1c−e). The structure of URAT1^{EM} obeys the classic MFS fold,[44,45] comprising 12 transmembrane helices (TMs), which are separated into an N-domain (TM1−6) and a C-domain (TM7−12), a glycosylated extracellular domain (ECD) between TM1 and TM2, and an intracellular four-helix bundle under the N-domain (Figure S5a). The N- and C-domains closely engage with each other on the extracellular side while opening a V-shaped central cavity facing the cytosol, elucidating that these structures were captured in an inward-facing state (Figure S5a). Structure superpositions reveal that URAT1 shares a high degree of structural similarity to other SLC22 transporters, reflected by small root-mean-square deviation (RMSD) values of 1.5 Å between URAT1^{EM} and rat OAT1 (PDB code 8SDU)[23] over 465 Cα atoms and of 1.7

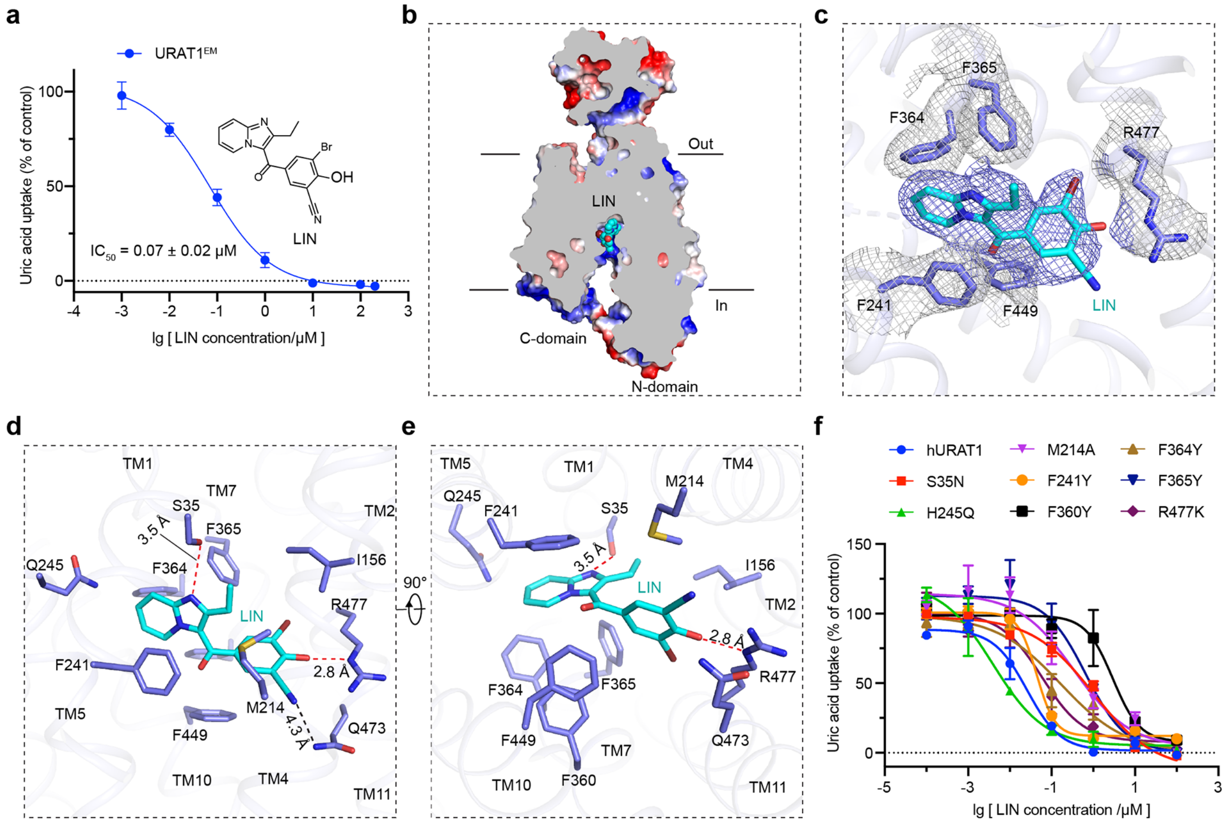

g

	hURAT1	S35N	H245Q	M214A	F241Y	F360Y	F364Y	F365Y	R477K
IC_{50} (μM)	0.026 ±0.007	1.005 ±0.317	0.004 ±0.002	0.349 ±0.239	0.044 ±0.010	2.944 ±1.301	0.167 ±0.117	0.663 ±0.298	0.059 ±0.030
Fold (/hURAT1)		39	0.15	13	1.7	113	6	26	2

Figure 3. Lingdolinurad binding site in URAT1. (a) Concentration-dependent inhibition of URAT1^{EM} by lingdolinurad. Data are normalized and presented as mean ± s.e.m.; $n = 3$ independent replicates. The chemical structure of lingolinurad is presented. (b) Cut-open electrostatic potential surface of URAT1^{LIN}. Positive and negative potentials are colored in blue and red, respectively. Lingdolinurad is depicted in cyan sticks. (c) EM density map for lingolinurad. The densities for lingolinurad and surrounding residues are shown in a blue and gray mesh, respectively. (d, e) Detailed lingolinurad site in URAT1. The side chains of residues involved in lingolinurad binding are shown as sticks. Red dashed lines indicate potential hydrogen bond interactions. (f, g) Inhibition of human URAT1 (hURAT1) WT and variants by lingolinurad. Cells were incubated with either an assay buffer or a gradient of lingolinurad for 5 min before exposure to 250 μM urate for 15 min. The basal uptake levels of GFP-expressing cells were subtracted. Data are normalized to their respective activities without lingolinurad and presented as mean ± s.e.m.; $n = 3$ independent replicates.

Å between URAT1^{EM} and human OCT1 (PDB code 8SC1)[27] over 388 Cα atoms (Figure S5b,c).

The central cavity of URAT1 is lined by TMs 1, 4, and 5 from the N-domain and TMs 7, 10, and 11 from the C-domain, which constitute the urate recognition site and translocation pathway (Figure S5a). The positively charged cavity is similar to that of OAT1 and is opposite to OCT1 because URAT1 and OATs prefer organic anions while OCTs transport organic cations (Figure S5d−f). Despite the overall structural similarity, the residues residing in the central cavity of URAT1 display critical differences compared to those in OAT1 and OCT1 (Figure S5g−i). We could not obtain the urate-bound URAT1 structure, presumably because of the urate's relatively low affinity (Figure 1a) or because the 1 mM urate concentration that we used may not have been high enough compared to other recently published studies.[34,36] Interestingly, previous findings suggest that Ser35 and Phe365 are necessary for the interaction with urate,[40] and Phe360, Gly361, and Arg477 are critical for urate transport.[38] In the URAT1 structures, these residues shape the interior of the cavity and interact with the inhibitors (Figure S5g). Moreover, Ser35, Phe360, Gly361, and Phe365 are not conserved in OAT1 or OCT1 (Figures S5g−i and S6), further indicating that these residues have an important role in urate recognition. In line with these observations, the mutations F241A, F360A, and F365A almost completely abolished URAT1 activity, and F360A, F449A, and R477A also greatly reduced transport activity; meanwhile, the mutants M214A and H245Q retained ~70% activity (Figure S5j).

URAT1 Inhibition by Benzbromarone

Benzbromarone (BEN) is a potent inhibitor of URAT1 and has long been used in treating gout.[46] Our concentration-dependent inhibition assay reveals that BEN has a half-maximal inhibitory concentration (IC_{50}) value of 425 nM in URAT1^{EM} (Figure 2a), which is approximately 2-fold of the reported IC_{50}

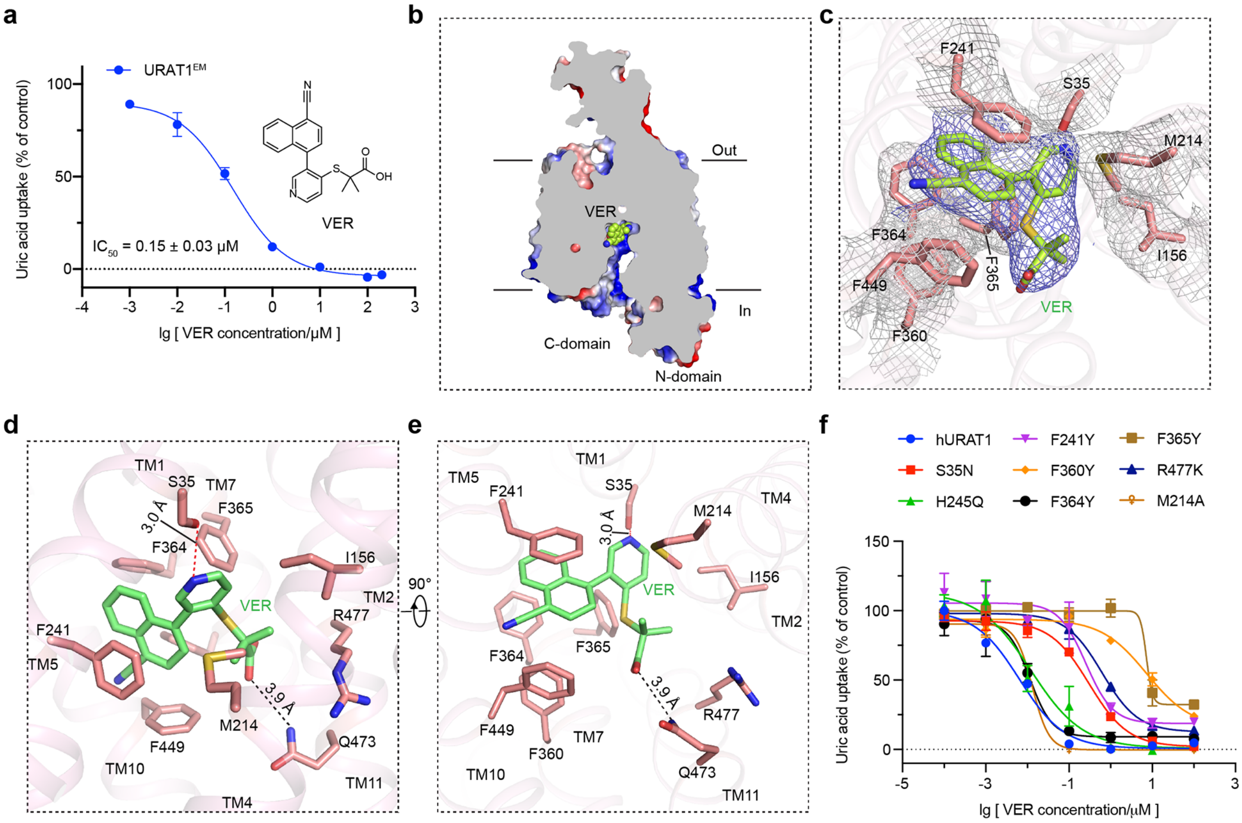

g

	hURAT1	S35N	H245Q	M214A	F241Y	F360Y	F364Y	F365Y	R477K
IC_{50} (μM)	0.006 ±0.002	0.304 ±0.055	0.012 ±0.007	0.013 ±0.001	0.254 ±0.130	7.332 ±3.714	0.011 ±0.004	~7.248 ±7431	0.620 ±0.120
Fold (/hURAT1)		51	2	2	42	1222	1.8	~1208	103

Figure 4. Verinurad binding site in URAT1. (a) Concentration-dependent inhibition of URAT1^{EM} by verinurad. Data are normalized and presented as mean ± s.e.m.; $n = 3$ independent replicates. The chemical structure of verinurad is presented. (b) Cut-open electrostatic potential surface of URAT1^{VER}. Positive and negative potentials are colored in blue and red, respectively. Verinurad is depicted in green sticks. (c) EM density map for verinurad. The densities for verinurad and surrounding residues are shown in a blue and gray mesh, respectively. (d, e) Detailed verinurad site in URAT1. The side chains of residues involved in verinurad binding are shown in the sticks. Red dashed lines indicate potential hydrogen bond interactions. (f, g) Inhibition of human URAT1 WT and variants by verinurad. Cells were incubated with either an assay buffer or a gradient of verinurad for 5 min before being exposed to 250 μM urate for 15 min. The basal uptake levels of GFP-expressing cells were subtracted. Data are normalized to their respective activities without verinurad and presented as mean ± s.e.m.; $n = 3$ independent replicates.

value of 220 nM in hURAT1.[40] To unravel the binding site of BEN in URAT1, we purified URAT1^{EM} with the addition of 10 μM BEN and determined the complex structure (URAT1^{BEN}) at 3.2 Å (Figure 1c and Figure S2). In the inward-facing URAT1^{BEN}, BEN resides in the central cavity, touching the top interior (Figures 1c and 2b). Strong EM densities allowed accurate assignments of BEN and surrounding residues (Figure 2c). BEN engages in multiple polar and nonpolar interactions with surrounding residues (Figure 2d,e). Specifically, the 3,5-dibromo-4-hydroxyphenyl ring is embraced by a phenylalanine tetrad of Phe241 on TM5, Phe360 and Phe364 on TM7, and Phe449 on TM10, and one of the bromide atoms forms a hydrogen bond interaction with Gln245 from TM5. Additionally, the benzofuran ring is sandwiched by Met214 on TM4 and Phe365 on TM7 with the contributions of hydrophobic interactions from Leu153 and Ile156 on TM2 as well as weak interaction from Arg477 on TM11. Sequence alignments demonstrate that these key residues in URAT1^{EM} are conserved in hURAT1 but not in other SLC22 transporters (Figure S7). Tan's study[40] revealed that substituting Ser35 and Phe365 of hURAT1 with Asn35 and Tyr365 from rURAT1 decreased the inhibitory potency of BEN by 10- and 17-fold, respectively. From the URAT1^{EM} structure, the mutations S35N and F365Y would reduce the pocket space, thus hindering BEN's binding to its site and decreasing the potency (Figure S8b). A third mutation, I481M, reduced BEN potency by 5-fold; however, Ile481 points out of the cavity and has no direct contact with the inhibitor, suggesting that Ile481 may indirectly affect BEN binding through interacting with other residues or affect protein stability (Figure S8b).

To verify the binding model of BEN in URAT1, we mutated the residues interacting with BEN and examined the sensitivity of the mutants to benzbromarone. Mutations including F241A, F364A, and F365A have no urate transport activity and thus are excluded from this test (Figure S5j). However, these mutants have expression and solution behavior similar to hURAT1 based on fluorescence-detection size-exclusion chromatography (FSEC) profiles (Figure S6). As illustrated in Figure 2f,g, benzbromarone inhibitory effects on M214A, F241Y, F360Y, F364Y, and R477K are decreased by 3-, 1.2-, 43-, 4.5-, and 11-fold, consistent with the finding of a previous study showing that the mutation R477K reduced the potency of BEN in hURAT1 by 4-fold. At the same time, F241Y increased the IC_{50} by 2-fold.[17] Furthermore, mutating Ser35 of hURAT1 to Asn35, or Phe365 to Tyr365 as found in rURAT1, caused a significant 10-fold or 25-fold increase in the IC_{50} value (Figure 2f,g). Interestingly, the substitution of hURAT1 His245 with glutamine from rURAT1, which forms a hydrogen bond with BEN in $URAT1^{BEN}$ (Figure 2d), has a negligible effect on urate transport and increases BEN sensitivity by ~2-fold (Figure S5j and Figure 2g), suggesting that His245 could have a similar role in urate and BEN recognition to Glu245. Collectively, these findings indicate that benzbromarone occupies the urate binding site and stabilizes URAT1 in the inward-facing state, thereby inhibiting URAT1 activity.

URAT1 Inhibition by Lingdolinurad

Lingdolinurad (LIN) is undergoing phase II clinical trials (NCT04638543) for treating gout.[13] LIN has an IC_{50} value of 70 nM in $URAT1^{EM}$, which is 6-fold more potent than BEN in inhibiting $URAT1^{EM}$ (Figures 2a and 3a). To define the detailed binding site of LIN, we solved the structure of $URAT1^{EM}$ in complex with LIN ($URAT1^{LIN}$) at 3.4 Å (Figure 1d and Figure S3). $URAT1^{LIN}$ was captured in the inward-facing state, the overall structure of which is nearly identical to $URAT1^{BEN}$ with a small RMSD value of 0.35 Å (Figures S3b and S7a). Strong EM density in the central cavity unequivocally elucidates a LIN molecule bound to URAT1 (Figure 3c). More precisely, the imidazo[1,2-*a*]pyridine ring is encircled by the phenylalanine tetrad of Phe241, Phe360, Phe364, and Phe449 and Thr32, Met36, and Gln245; a hydrogen bond interaction between the nitrogen atom in the imidazole ring and Ser35 is observed, which is absent in $URAT1^{BEN}$ (Figure 3d). In addition, the hydroxy benzonitrile group forms a strong hydrogen bond interaction with Arg477 and relatively weak polar interactions with Gln473 (Figure 3d,e), such interactions are not present in $URAT1^{BEN}$. Structure-guided point mutagenesis analysis elucidates that the mutations M214A, F241Y, F360Y, and F364Y all reduced the inhibitory effects of LIN by 13-, 1.7-, 113-, and 6-fold, respectively; especially the mutations M214A and F360Y are more critical (Figure 3f,g). Specifically, mutating Ser35 of hURAT1 to Asn35 or Phe365 to Tyr365 of rURAT1 caused a roughly 39- or 26-fold decrease in LIN inhibitory effects, respectively, indicating that the hydrogen bond interaction between Ser35 and LIN is critical for LIN binding (Figure 3f,g). The R477K mutation only caused a 2-fold decrease, probably because the lysine residue can still form proper interaction with LIN. Of note, substituting His245 of hURAT1 to a rURAT1 Gln245 increased the potency of LIN, suggesting that Gln245 in $URAT1^{EM}$ may have a more important contribution to LIN binding than does His245 in hURAT1. The superposition of the LIN and BEN binding sites reveals that LIN and BEN occupy a largely overlapped region in URAT1, and most of the residues involved in LIN binding are identical to those with BEN (Figure S8c), partially owing to the structural similarity between the two inhibitors (Figures 2a and 3a). Surprisingly, their binding poses are distinct: LIN underwent a 180° rotation parallel to the membrane plane relative to BEN; additionally, Met214, Phe449, and Arg477 rotate their side chains to accommodate the respective inhibitors (Figure S8c). Notably, the guanidine group of Arg477 moves away from the cavity to create space for accommodating the hydroxy benzonitrile moiety of LIN. The higher potency of LIN than BEN is presumably because of two additional hydrogen bond interactions between LIN and Ser35 and Arg477. Based on these findings, LIN binds to a similar site to that of BEN in URAT1 and locks URAT1 in the inward-facing conformation.

URAT1 Inhibition by Verinurad

Verinurad (VER) is a highly potent and specific URAT1 inhibitor for treating hyperuricemia and gout,[17] which is at least hundreds of times more potent than in human OATs and rat URAT1. We show that VER has an IC_{50} value of 150 nM in inhibiting $URAT1^{EM}$ (Figure 4a), which is 6-fold less potent than the IC_{50} value of 25 nM in hURAT1.[17] To reveal the structural basis for the high potency and specificity of VER, we determined the complex structure of $URAT1^{EM}$ bound to VER ($URAT1^{VER}$) at 3.5 Å (Figure 1e and Figure S4). The overall structure of $URAT1^{VER}$ is highly similar to $URAT1^{BEN}$ and $URAT1^{LIN}$ (Figure S8a). Still, the shape of the extra density in the central cavity of $URAT1^{VER}$ is somewhat different from that in the other two structures (Figure 1c−e), indicating the binding of a VER molecule to the inward-facing $URAT1^{VER}$ (Figure 4b,c). Structural analysis suggests that most of the important residues interacting with BEN and LIN are involved in constituting the pocket of VER (Figure S8d,e). The naphthalene double ring is cradled by the phenylalanine tetrad; the pyridine ring is clamped by the Met214 and Phe365 pair, of which the nitrogen atom engages in a hydrogen bond interaction with Ser35; moreover, the carboxyl group interacts with Gln473, while Arg477 is positioned at the closest distance of 5.2 Å to the carboxyl group, suggesting that Gln473 might contribute more for interaction (Figure 4d,e).

The previous findings have revealed that the mutations S35N and F365Y reduce the potency of VER in hRUAT1 by 14- and 160-fold,[17] respectively, suggesting that Ser35 and Phe365, which are not conserved in rURAT1 and human OATs, are the most important determinants for the potency and specificity of VER. The $URAT1^{VER}$ structure demonstrates that Ser35 contributes a hydrogen bond, and Phe365 stabilizes the binding coupled with Met214 (Figure 4d,e). Our point mutagenesis functional assay indicates that the mutations M214A, F241Y, F360Y, and R477K impaired the inhibition of VER by 2-, 42-, 1222-, and 103-fold IC_{50} changes, respectively (Figure 4f,g). In particular, the S35N and F365Y mutants of hURAT1 caused a 50- or 1200-fold increase in the IC_{50} value compared with WT hURAT1, while the H245Q mutation resulted in a slightly 2-fold increase (Figure 4f,g), highlighting the important roles of S35 and F365 in VER recognition. VER binds to a pocket similar to that of BEN and LIN in URAT1, which is shaped by the same residues with subtle conformational changes (Figure S8c−e). Thus, our structures have defined a bona fide pocket for binding inhibitors, especially for those with a two-ring and one-ring conjunction.

MD Simulation Analysis of the Inhibitor Binding in URAT1

To gain insights into the dynamics and the binding differences of the inhibitors interacting with URAT1, we conducted all-atom molecular dynamics (MD) simulations using the structures of $URAT1^{BEN}$, $URAT1^{LIN}$, and $URAT1^{VER}$ as an initial model, respectively. During the 400 ns MD simulation of three independent repeats, the simulation for each of the three inhibitors reached a steady state, demonstrating that the overall

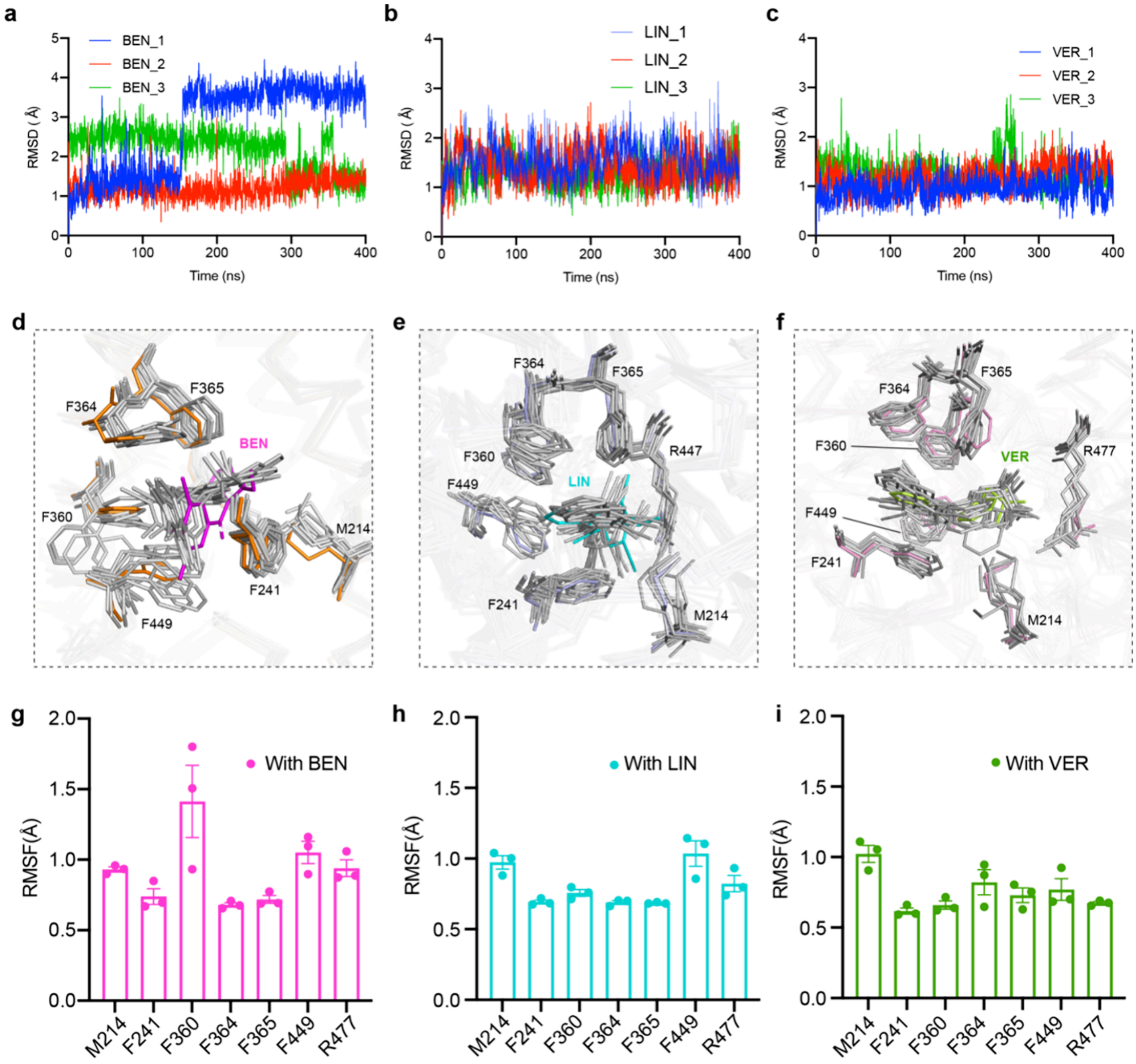

Figure 5. MD simulation of inhibitor binding in URAT1. (a−c) RMSD of BEN (a), LIN (b), and VER (c) plotted for three independent 400 ns MD simulations. (d−f) Close-up view of the BEN (d), LIN (e), and VER (f) and binding sites showing the cryo-EM model and the representative conformations of the simulation replicas. (g−i) Key residues' root-mean-square fluctuation (RMSF) of BEN (g), LIN (h), and VER (i) plotted for three independent 400 ns MD simulations.

binding poses of the three inhibitors appear to be relatively tight, and BEN is more dynamic than LIN and VER, reflected by the RMSD of BEN within 4 Å while the RMSD of the other two inhibitors is within 2 Å (Figure 5a−c). We next analyzed eight representative trajectories of each inhibitor and superimposed them with the respective structure, showing that BEN and interacting residues, including Phe360 and Phe499, could adopt different conformations, but LIN and VER are relatively more stable (Figure 5d−f). Consistent with this, per-residue root-mean-square fluctuation (RMSF) analyses suggest that Phe360 of URAT1^{BEN} has the highest RMSF values among all the tested residues (Figure 5g−i). These MD analysis results align with the lowest potency of BEN in inhibiting URAT1^{EM} (Figures 2a, 3a, and 4).

■ CONCLUSIONS

Uric acid is the end product of purine metabolism, and a high level of SUA is a non-negligible risk causing various pathological conditions, including gout.[5,47,48] Urate is mainly excreted in the kidney, and blocking the renal reabsorption of urate can lower SUA levels and potentially alleviate hyperuricemia-associated conditions; hence, uricosurics such as probenecid, benzbromarone, sulfinpyrazone, and lesinurad have been clinically used in treating hyperuricemia and gout, and many novel URAT1 inhibitors are emerging,[19−21] highlighting the potential of URAT1 as an important drug target. In this study, we selected three representative URAT1 inhibitors and investigated the structural basis of their modes of action in inhibiting URAT1. Initially, we found that the unstable human wild-type URAT1 samples impede structural analysis. Instead, the introduction of the three human mutations (N35S, Y365F, and M481I) to rat URAT1 not only improves sample stability but also restores high affinity to urate and inhibitors.[40] We, therefore, successfully determined the humanized rURAT1 structures in complex with benzbromarone, verinurad, and lingdolinurad. Structural analyses reveal that most residues constituting the central cavity of URAT1^{EM} are identical to those in human URAT1, suggesting that these structures could serve as valuable templates for structure-based drug design. Comparing URAT1^{EM} with OAT1 and OCT1 of the SLC22 family elucidates that the nonconserved Ser35, Phe360, and Phe365 are positioned at the apex of the interior, and Arg477 could donate a positive charge for interacting with the negative charge of UA, which together define urate recognition. The important role of Arg477 has been demonstrated in recently published studies,[34,36] although the orientation of urate is not consistent (Figure S9). The binding mode of urate in Wu et al.'s study (PDB code 9JDV)[37] is even more different, probably due to the opening differences of URAT1 and distinct conformations of Arg477 and Phe241 (Figure S9). These findings suggest that the urate binding pocket is relatively flexible.

The inhibitor-bound complex structures clearly demonstrate the detailed binding modes for the three inhibitors, which all bind to a similar region and stabilize URAT1 in the inward-facing state. This observation is consistent with previous competitive inhibition results, suggesting that VER, BEN, sulfinpyrazone, and probenecid bind to a similar site in URAT1.[17] Indeed, we have mapped the hot spots in URAT1 for drug binding: the phenylalanine tetrad of Phe241, Phe360, Phe364, and Phe449 constitute a hydrophobic pocket for accommodating hydrophobic moieties with one or two rings; the hydrophobic pair of Met214 and Phe365 bears a distance of 8 Å and could tightly catch a ring-like group of bound inhibitors between them; moreover, surrounding hydrophilic residues such as Ser35, Gln245 (His245 in hURAT1), Asp389, Gln473, and Arg477 could form hydrogen bond or electrostatic interactions with the branches on the inhibitors. These residues are not fully conserved in URAT1 from different species or other SLC22 members. For instance, the uricosurics (probenecid, benzbromarone, sulfinpyrazone, and lesinurad) are at least 100-fold more potent in inhibiting hURAT1 than rURAT1, which is mainly determined by Ser35 and Phe365 of hURAT1.[40] Additionally, the Met214/Phe365 pair is not conserved in OATs or OCTs.

Recently, several papers reported URAT1 bound with substrates or inhibitors.[33−37] Consistent with our results, these studies also found that the purified WT human URAT1 is aggregated. To facilitate the structural study, Dai and Lee engineered the human URAT1 by replacing the intracellular loop between TM6 and TM7 of URAT1 (residues 280−343) with the corresponding sequence from human OAT4 (residues 277−339) and the extracellular loop between TM1 and TM2 of URAT1 (residues 60−65) with the corresponding sequence from OAT4 (residues 60−62).[34] Guo et al. engineered hURAT1 via consensus design, which included 15 designed mutations located on the periphery of hURAT1.[36] Suo et al. also employed the consensus design, introducing more than 50 mutations, resulting in a chimeric URAT1 with 91% sequence identity to hURAT1.[35] Interestingly, Wu et al. reported the WT URAT1 structures;[37] however, their maps have a relatively lower resolution than other reports. Although different protein engineering strategies were employed, the resulting drug-bound structures are similar: benzbromarone and verinurad bound to the central pocket of the inward-open URAT1. However, the detailed binding poses are different. When comparing these benzbromarone-bound URAT1 structures, we found that the BEN orientation in our structure is similar to that of Suo et al. (Figure S10a,b), whereas Guo et al. and Wu et al. reported the BEN orientation displaying a 180° flip parallel to the membrane (Figure S10c−g), suggesting that the central binding pocket of URAT1 has some degree of plasticity. In contrast to BEN, the binding mode differences of VER are smaller, with some flexibility observed in the naphthalene double ring and the carboxyl group of VER, while the pyridine ring remains stable in the structures of these studies[34,36,37] (Figure S11a−c). Still, we observed an ∼45° counterclockwise rotation of the naphthalene double ring group in our VER binding mode and an ∼145° clockwise rotation of Phe241 to accommodate and interact with VER (Figure S11d−i). These observations further demonstrate that the central pocket of URAT1 can bind different types of ligands via adjusting local conformation changes. It is worth noting that the differences in the binding modes of the inhibitors could arise from the different protein engineering strategies. In addition to benzbromarone and verinurad, we also presented the complex structures of URAT1 bound to lingdolinurad, which was not reported in other studies. Lingdolinurad, developed by Atom Therapeutics, reduces renal reabsorption of uric acid by inhibiting URAT1 and is currently undergoing multicenter phase 2b/3 clinical trials worldwide, including in China and the United States (NCT05818085).[49] Given that structures with several small molecules are now available and can be utilized for docking, one might assume that the binding modes of these small molecules would be very similar. However, we found that their binding poses are surprisingly distinct. Specifically, lingdolinurad underwent a 180° rotation parallel to the membrane plane relative to benzbromarone. These findings underscore the ongoing interest in the structures of lingdolinurad, particularly given the relevance of URAT1 inhibitors in treating hyperuricemia-associated diseases.

METHODS

Expression and Purification of URAT1

The genes of full-length wild-type URAT1 of humans (UniProt accession code: Q96S37) and rats (UniProt accession code: Q3ZAV1) were inserted into a pEG2 vector with a Twin-Strep tag, a green fluorescent protein (GFP), and an HRV 3C protease site fused at the N-terminus. The EM construct contains a GFP-specific nanobody fused at the C-terminus of URAT1. All mutations were generated by the standard site-directed mutagenesis methods using the Mut Express II Fast mutagenesis kit (Vazyme Biotech Co., Ltd.). All constructs of URAT1 and mutants were confirmed by DNA sequencing. For large-scale protein expression, the plasmids were first transformed into DH10bac cells (Thermo Fisher) to produce bacmids. Then, purified bacmids were transduced into *Spodoptera frugiperda* (Sf9) insect cells to produce the baculoviruses using the Bac-to-Bac baculovirus expression system (Invitrogen). P2 baculoviruses were amplified in *Sf*9 cells and were collected for protein expression. HEK293F (Gibco, USA) cells were cultured in an OPM-293 medium (OPM, China) in a 37 °C incubator supplemented with 5% CO_2 and shaking at 120 rpm. When cells grow to a density of approximately 2.5×10^6 cells/mL, P2 baculoviruses are added to the medium at a ratio of 1:100 (v/v). To increase protein expression, filtered sodium butyrate (Sigma, USA) was added to the medium 12 h after transfection at a final concentration of 10 mM. Cells were cultured for another 48 h and then were harvested by centrifugation at 2000*g* for 3 min. The cell pellets were stored at −80 °C.

For purification of URAT1^{EM}, cell pellets were resuspended in buffer A containing 20 mM HEPES, pH 7.5, 150 mM NaCl, 2 mM β-mercaptoethanol (β-ME), and protease inhibitors, including 1 mM phenylmethylsulfonic acid acyl fluoride (PMSF), 0.8 μM pepstatin, 2 μM leupeptin, and 2 μM aprotinin. Cells were manually broken in a glass Dounce homogenizer on ice. Membrane fractions were collected by ultracentrifugation at 100,000 g for 60 min. They were resuspended in buffer A supplemented with 1% (w/v) *n*-dodecyl-β-D-maltoside (DDM, Anatrace, USA) and 0.15% (w/v) cholesterol hemisuccinate (CHS, Anatrace, USA). Cell membrane proteins were solubilized for 1.5 h at 4 °C. To remove insoluble debris, a second ultracentrifugation was performed at 100,000 g for 30 min. Then, the supernatant was subjected to Streptactin beads (Smart-Lifesciences, China) twice by gravity flow at 4 °C. After being washed with 10 column volumes of wash buffer B (buffer A supplemented with 0.01% (w/v) lauryl maltose neopentyl glycol (LMNG, NG310, Anatrace), the URAT1^{EM} samples were eluted with 5 mL of buffer B supplemented with 5 mM desthiobiotin (Sigma, USA). Subsequently, the protein was concentrated and subjected to a Superose 6 increase 10/300 GL column (Cytiva) equilibrated with buffer C containing 20 mM Hepes, pH 7.5, 150 mM NaCl, 2 mM β-ME, and 0.001% (w/v) LMNG. The peak fractions were concentrated to 15 mg/mL for cryo-EM grid preparation. For each purification of URAT1−inhibitor complexes, inhibitors were added to the purification buffers and to the gel filtration buffers at a concentration of 10 μM.

Urate Transport Assay

To assess urate transporting, we adapted an LC-MS/MS-based approach from a previous report.[50] The main differences include that HEK293T cells transfected with Vector, URAT1^{EM}, hURAT1, and hURAT1_mutants were used for the analysis and some modifications with LC-MS/MS methods. For LC-MS analysis of metabolites, samples were analyzed by reversed-phase liquid chromatography on an ACQUITY UPLC I-Class system using an ACQUITY UPLCBEH C18 1.7 μm column (2.1 × 100 mm, 1.8 μm) (Waters). Water with 0.1% formic acid (A) and acetonitrile with 0.1% formic acid (B) were used as the mobile phase components at a flow rate of 0.2 mL/min. For the analysis of uric acid, the 5 min gradient method was used as follows: 0−2 min, 5% B; 2−4 min, 95% B; 4−5 min, 5% B. One μL of the sample was injected.

Uric acid and uric acid-$^{15}N_2$ were quantified by multiple reaction monitoring (MRM) *m/z* 167/124, 167/96, 169/126, and 169/98 analysis. GraphPad Prism software was used for nonlinear regression and statistical analysis after subtracting basal uptake measurement from GFP-expressing cells.

Cryo-EM Sample Preparation and Data Collection

Before sample preparation, the purified URAT1 samples were supplemented with 1 mM variant inhibitors and incubated for 1 h on ice. After centrifugation at 18,000 g (M1324R, RWD) for 20 min at 4 °C, aliquots of 3.0 μL samples were applied to glow-discharged holey carbon grids (Quantifoil, 300 mesh, R1.2/1.3, Cu). After waiting for 30 s, grids were blotted for 2.0−4.0 s at 4 °C with 100% humidity and plunged into liquid nitrogen-cooled liquid ethane by using a Vitrobot Mark IV (Thermo Fisher Scientific).

All cryo-EM data sets were collected using a 300 kV Titan Krios G4 microscope (Thermo Fisher Scientific) equipped with a K3 direct electron detector and a GIF quantum energy filter (Gatan) with a slit of 10 mV. After manual inspection of grid quality, all movie stacks were automatically acquired using EPU (Thermo Fisher Scientific) at a nominal magnification of 105,000 with a physical pixel size of 0.85 Å. The dose rate was adjusted to 15 counts/pixel/s. Each movie stacks were fractioned into 40 frames with an exposure time of 2.69 s. The total dose is 60 e/Å^2. The defocus range was set between −1.0 and −2.0 μm. A total of 3363, 2754, and 2660 movie stacks were collected for URAT1^{BEN}, URAT1^{LIN}, and URAT1^{VER}, respectively.

Cryo-EM Data Processing

All movie stacks were imported into CryoSPARC[51] and performed patch motion correction and contrast transfer function (CTF) estimation. After selecting micrographs with CTF fitting better than 4 Å, a total of 3,694,288, 3,452,476, and 3,849,172 particles were automatically picked by Blob Picker with a minimum diameter of 90 Å and a maximal diameter of 120 Å for URAT1^{BEN}, URAT1^{LIN}, and URAT1^{VER}, respectively. Particles were extracted and were subjected to several rounds of 2D classification to remove junk particles, resulting in 740,315, 745,590, and 377,377 good particles for URAT1^{BEN}, URAT1^{LIN}, and URAT1^{VER}, respectively. Next, ab initio reconstruction was conducted to generate an initial 3D model. After several rounds of heterogeneous refinements with good models and junk models as references, a final round of 69,925, 88,684, and 60,262 particles for URAT1^{BEN}, URAT1^{LIN}, and URAT1^{VER} were kept and were re-extracted for nonuniform refinement. Finally, EM maps for URAT1^{BEN}, URAT1^{LIN}, and URAT1^{VER} at 3.2, 3.4, and 3.5 Å, respectively, were achieved from local refinement with a local mask covering the TMD region. The detailed flowcharts of cryo-EM data processing are presented in Figures S2−S4.

Model Building and Refinement

The predicted AlphaFold2 model of rat URAT1 was manually fitted into the EM density map of URAT1^{BEN} in Chimera[52] and was manually inspected and corrected in Coot.[53] Model refinement of URAT1^{BEN} using the cryo-EM map was performed using the phenix.real_space_refine in Phenix.[54] After model refinement, the inhibitor was manually fitted into the extra densities within the map. The models were further refined in Phenix, and the FSC curve was calculated by Phenix.mtrage. For URAT1^{LIN} and URAT1^{VER}, the URAT1^{BEN} structure was manually fitted into their respective EM maps in Chimera. Then, the models were corrected in Coot and refined in Phenix, as described above. The statistics of cryo-EM data collection and model refinement are summarized in Table S1. All figures were prepared with ChimeraX[55] and PyMol (Schrödinger, LLC).

FSEC for URAT1

HEK293T cells were cultured to ∼70% confluency in a 6-well plate and transiently transfected with the specific URAT1 constructs (3 μg/well) by using PEI (polyethylenimine linear, MW 40,000). After incubating for 24 h, the cells were harvested by centrifugation and resuspended in 200 μL of a solubilization buffer, the same as used for protein purification. The mixture was rotated for 1 h at 4 °C followed by centrifugation at 45,000*g* for 20 min. For fluorescence-detection size-exclusion chromatography (FSEC), the supernatant fraction (30 μL) was loaded onto a Superose 6 column. The eluent from the SEC column was passed through a fluorometer fitted with a flow cell.

Molecular Dynamics Simulation

The bilayer membrane system with protein complexes was prepared using the CHARMM-GUI.[56] All complexes were merged into the POPC bilayer membrane and solvated in water with 150 mM NaCl. We used the Amber ff19SB force field for the protein, the TIP3P force field for the waters, the Lipid21 parameter for POPC in the bilayer membrane, and the gaff2 parameter for ligands in the complex. The simulation was done by Amber20 and AmberTools21.[57] The particle mesh Ewald method with periodic boundary conditions was used to model long-range electrostatic effects. A 9 Å cutoff was applied to Lennard-Jones and electrostatic interactions. The SHAKE algorithm was used to constrain the bonds containing hydrogen. For each system, three independent simulations were performed in the following steps: (1) Minimization was performed without the SHAKE algorithm with a maximum cycle of 10,000 and with the steepest descent algorithm for the first 5000 cycles. Position restraints of 5 kcal mol^{-1} Å^{-2} were applied to the protein and the ligand. (2) Minimization was performed without the SHAKE algorithm with a maximum cycle of 10,000 and with the steepest descent algorithm for the first 5000 cycles. (3) The temperature was increased to 310 K in 1 ns with a periodic boundary for constant volume by Langevin dynamics with a collision frequency of 2 ps^{-1}. (4) A 1 ns density equilibrium with a periodic boundary for constant pressure was performed, and Berendsen's coupling was used to maintain the system's pressure at 1 bar with semi-isotropic pressure scaling. (5) A 400 ns production with a periodic boundary for constant pressure and a constant temperature of 310 K was performed. VMD was used to analyze the MD trajectories.[58]

ASSOCIATED CONTENT

Data Availability Statement

The three-dimensional cryo-EM density maps of URAT1^{BEN}, URAT1^{LIN}, and URAT1^{VER} have been deposited into the Electron Microscopy Data Bank under accession numbers EMD-61155 [https://www.emdataresource.org/EMD-61155], EMD-61156 [https://www.emdataresource.org/EMD-61156], and EMD-61157 [https://www.emdataresource.org/EMD-61157], respectively. The coordinates of URAT1^{BEN}, URAT1^{LIN}, and URAT1^{VER} have been deposited into the Protein Data Bank under accession codes 9J5W [10.2210/pdb9J5W/pdb], 9J5X [10.2210/pdb9J5X/pdb], and 9J5Z [10.2210/pdb9J5Z/pdb], respectively.

Supporting Information

The Supporting Information is available free of charge at https://pubs.acs.org/doi/10.1021/jacsau.4c01188.

> Optimization and purification of URAT1; cryo-EM data processing of URAT1; structural features of URAT1; protein FSEC profile; sequence alignment and structural comparisons of URAT1 structures (PDF)

AUTHOR INFORMATION

Corresponding Authors

Junping Fan − *Beijing National Laboratory for Molecular Sciences, Key Laboratory of Bioorganic Chemistry and Molecular Engineering of Ministry of Education, Institute of Organic Chemistry, College of Chemistry and Molecular Engineering, Peking University, Beijing 100871, China;* orcid.org/0000-0002-2615-8098; Email: fanjp@pku.edu.cn

Xiaoguang Lei − *Beijing National Laboratory for Molecular Sciences, Key Laboratory of Bioorganic Chemistry and Molecular Engineering of Ministry of Education, Institute of Organic Chemistry, College of Chemistry and Molecular Engineering and Peking-Tsinghua Center for Life Sciences, Peking University, Beijing 100871, China; Institute for Cancer Research, Shenzhen Bay Laboratory, Shenzhen 518107, China;* orcid.org/0000-0002-0380-8035; Email: xglei@pku.edu.cn

Authors

Wenjun Xie − *Beijing National Laboratory for Molecular Sciences, Key Laboratory of Bioorganic Chemistry and Molecular Engineering of Ministry of Education, Institute of Organic Chemistry, College of Chemistry and Molecular Engineering and Peking-Tsinghua Center for Life Sciences, Peking University, Beijing 100871, China*

Han Ke − *Beijing National Laboratory for Molecular Sciences, Key Laboratory of Bioorganic Chemistry and Molecular Engineering of Ministry of Education, Institute of Organic Chemistry, College of Chemistry and Molecular Engineering, Peking University, Beijing 100871, China*

Jing Zhang − *Jiangsu JITRI Molecular Engineering Inst. Co., Ltd., Jiangsu 215500, China*

Jin Wang − *Beijing National Laboratory for Molecular Sciences, Key Laboratory of Bioorganic Chemistry and Molecular Engineering of Ministry of Education, Institute of Organic Chemistry, College of Chemistry and Molecular Engineering, Peking University, Beijing 100871, China*

Haijun Wang − *Beijing National Laboratory for Molecular Sciences, Key Laboratory of Bioorganic Chemistry and Molecular Engineering of Ministry of Education, Institute of Organic Chemistry, College of Chemistry and Molecular Engineering, Peking University, Beijing 100871, China*

Nianxin Guo − *Beijing National Laboratory for Molecular Sciences, Key Laboratory of Bioorganic Chemistry and Molecular Engineering of Ministry of Education, Institute of Organic Chemistry, College of Chemistry and Molecular Engineering, Peking University, Beijing 100871, China*

Yingjie Bai − *Institute for Cancer Research, Shenzhen Bay Laboratory, Shenzhen 518107, China*

Complete contact information is available at: https://pubs.acs.org/10.1021/jacsau.4c01188

Author Contributions

[‡]J.F., W.X., and H.K. contributed equally. X.L. initiated the project. X.L. and J.F. supervised the project. J.F. conceived and designed the experiments. W.X. made all the constructs under J.F.'s instruction. J.F. prepared protein samples for the cryo-EM study, collected and processed the cryo-EM data, and built and refined the models. J.F., W.X., and H.K. performed the uric acid transport assays. J.Z. and J.W. synthesized the compounds. H.W., N.G., and Y.B. helped with the LC-MS/MS detection. J.F. wrote the paper, and all authors reviewed and revised it. CRediT: **Junping Fan** data curation, formal analysis, investigation, methodology, project administration, resources, software, supervision, validation, visualization, writing - original draft; **Wenjun Xie** formal analysis, investigation, methodology, resources, validation, writing - review & editing; **Han Ke** formal analysis, investigation, resources, software, validation, visualization, writing - review & editing; **Jing Zhang** resources; **Jin Wang** resources; **Haijun Wang** methodology; **Nianxin Guo** methodology; **Yingjie Bai** methodology; **Xiaoguang Lei** conceptualization, funding acquisition, project administration, supervision, writing - review & editing.

Funding

This work is supported by the National Key Research & Development Plan (2022YFC2502500 to X.L.), the National Natural Science Foundation of China (22193073 and 92253305 to X.L.; 22177006 to J.F.), and the Beijing National Laboratory for Molecular Sciences (BNLMS-CXX-202106 to X.L.). X.L. is also supported by the New Cornerstone Science Foundation through the XPLORER PRIZE. A special research grant for biocatalyst development from Novartis Pharma AG for X.L. is acknowledged.

Notes

The authors declare no competing financial interest.

ACKNOWLEDGMENTS

We thank Dr. J. Zhao and Dr. B. Xu at the Cryo-EM Center of the School of Advanced Agricultural Sciences of Peking University for support in cryo-EM data collection and the cryo-EM platform of Peking University for support in cryo-EM sample preparation. Mass spectrometry was measured at the Analytical Instrumentation Center of Peking University. The help from Ms. Xia Liu and Dr. Zejun Li was acknowledged. We are grateful to the High-Performance Computing Platform of Peking University for the molecular dynamics simulations.

REFERENCES

(1) Maiuolo, J.; Oppedisano, F.; Gratteri, S.; Muscoli, C.; Mollace, V. Regulation of uric acid metabolism and excretion. *Int. J. Cardiol* **2016**, *213*, 8−14.

(2) Kratzer, J. T.; Lanaspa, M. A.; Murphy, M. N.; Cicerchi, C.; Graves, C. L.; Tipton, P. A.; Ortlund, E. A.; Johnson, R. J.; Gaucher, E. A. Evolutionary history and metabolic insights of ancient mammalian uricases. *Proc. Natl. Acad. Sci. U. S. A.* **2014**, *111* (10), 3763−3768.

(3) Ames, B. N.; Cathcart, R.; Schwiers, E.; Hochstein, P. Uric acid provides an antioxidant defense in humans against oxidant- and radical-caused aging and cancer: a hypothesis. *Proc. Natl. Acad. Sci. U. S. A.* **1981**, *78* (11), 6858−6862.

(4) Halperin Kuhns, V. L.; Woodward, O. M. Urate transport in health and disease. *Best Pract Res. Clin Rheumatol* **2021**, *35* (4), No. 101717.

(5) So, A.; Thorens, B. Uric acid transport and disease. *J. Clin Invest* **2010**, *120* (6), 1791−1799.

(6) Eraly, S. A.; Vallon, V.; Rieg, T.; Gangoiti, J. A.; Wikoff, W. R.; Siuzdak, G.; Barshop, B. A.; Nigam, S. K. Multiple organic anion transporters contribute to net renal excretion of uric acid. *Physiol Genomics* **2008**, *33* (2), 180−192.

(7) Dehghan, A.; Kottgen, A.; Yang, Q.; Hwang, S. J.; Kao, W. L.; Rivadeneira, F.; Boerwinkle, E.; Levy, D.; Hofman, A.; Astor, B. C.; et al. Association of three genetic loci with uric acid concentration and risk of gout: a genome-wide association study. *Lancet* **2008**, *372* (9654), 1953−1961.

(8) Tin, A.; Marten, J.; Halperin Kuhns, V. L.; Li, Y.; Wuttke, M.; Kirsten, H.; Sieber, K. B.; Qiu, C.; Gorski, M.; Yu, Z.; et al. Target genes, variants, tissues and transcriptional pathways influencing human serum urate levels. *Nat. Genet.* **2019**, *51* (10), 1459−1474.

(9) Woodward, O. M.; Kottgen, A.; Coresh, J.; Boerwinkle, E.; Guggino, W. B.; Kottgen, M. Identification of a urate transporter, ABCG2, with a common functional polymorphism causing gout. *Proc. Natl. Acad. Sci. U. S. A.* **2009**, *106* (25), 10338−10342.

(10) Vitart, V.; Rudan, I.; Hayward, C.; Gray, N. K.; Floyd, J.; Palmer, C. N.; Knott, S. A.; Kolcic, I.; Polasek, O.; Graessler, J.; et al. SLC2A9 is a newly identified urate transporter influencing serum urate concentration, urate excretion and gout. *Nat. Genet.* **2008**, *40* (4), 437−442.

(11) Enomoto, A.; Kimura, H.; Chairoungdua, A.; Shigeta, Y.; Jutabha, P.; Cha, S. H.; Hosoyamada, M.; Takeda, M.; Sekine, T.; Igarashi, T.; et al. Molecular identification of a renal urate anion exchanger that regulates blood urate levels. *Nature* **2002**, *417* (6887), 447−452.

(12) Toyoda, Y.; Takada, T.; Miyata, H.; Matsuo, H.; Kassai, H.; Nakao, K.; Nakatochi, M.; Kawamura, Y.; Shimizu, S.; Shinomiya, N.; et al. Identification of GLUT12/SLC2A12 as a urate transporter that regulates the blood urate level in hyperuricemia model mice. *Proc. Natl. Acad. Sci. U. S. A.* **2020**, *117* (31), 18175−18177.

(13) Jenkins, C.; Hwang, J. H.; Kopp, J. B.; Winkler, C. A.; Cho, S. K. Review of Urate-Lowering Therapeutics: From the Past to the Future. *Front Pharmacol* **2022**, *13*, No. 925219.

(14) Tatrai, P.; Erdo, F.; Dornyei, G.; Krajcsi, P. Modulation of Urate Transport by Drugs. *Pharmaceutics* **2021**, *13* (6), 899.

(15) Taniguchi, T.; Ashizawa, N.; Matsumoto, K.; Saito, R.; Motoki, K.; Sakai, M.; Chikamatsu, N.; Hagihara, C.; Hashiba, M.; Iwanaga, T. Pharmacological Evaluation of Dotinurad, a Selective Urate Reabsorption Inhibitor. *J. Pharmacol Exp Ther* **2019**, *371* (1), 162−170.

(16) Fujita, K.; Isozumi, N.; Zhu, Q.; Matsubayashi, M.; Taniguchi, T.; Arakawa, H.; Shirasaka, Y.; Mori, E.; Tamai, I. Unique Binding Sites of Uricosuric Agent Dotinurad for Selective Inhibition of Renal Uric Acid Reabsorptive Transporter URAT1. *J. Pharmacol Exp Ther* **2024**, *390* (1), 99−107.

(17) Tan, P. K.; Liu, S.; Gunic, E.; Miner, J. N. Discovery and characterization of verinurad, a potent and specific inhibitor of URAT1 for the treatment of hyperuricemia and gout. *Sci. Rep* **2017**, *7* (1), 665.

(18) Fitz-Patrick, D.; Roberson, K.; Niwa, K.; Fujimura, T.; Mori, K.; Hall, J.; Yan, X.; Shen, Z.; Liu, S.; Ito, Y.; et al. Safety and efficacy of verinurad, a selective URAT1 inhibitor, for the treatment of patients with gout and/or asymptomatic hyperuricemia in the United States and Japan: Findings from two phase II trials. *Mod. Rheumatol* **2019**, *29* (6), 1042−1052.

(19) Song, D.; Zhao, X.; Wang, F.; Wang, G. A brief review of urate transporter 1 (URAT1) inhibitors for the treatment of hyperuricemia and gout: Current therapeutic options and potential applications. *Eur. J. Pharmacol.* **2021**, *907*, No. 174291.

(20) Dong, Y.; Zhao, T.; Ai, W.; Zalloum, W. A.; Kang, D.; Wu, T.; Liu, X.; Zhan, P. Novel urate transporter 1 (URAT1) inhibitors: a review of recent patent literature (2016−2019). *Expert Opin Ther Pat* **2019**, *29* (11), 871−879.

(21) Shi, X.; Zhao, T.; da Silva-Junior, E. F.; Zhang, J.; Xu, S.; Gao, S.; Liu, X.; Zhan, P. Novel urate transporter 1 (URAT1) inhibitors: a review of recent patent literature (2020-present). *Expert Opin Ther Pat* **2022**, *32* (12), 1175−1184.

(22) Nigam, S. K. The SLC22 Transporter Family: A Paradigm for the Impact of Drug Transporters on Metabolic Pathways, Signaling, and Disease. *Annu. Rev. Pharmacol Toxicol* **2018**, *58*, 663−687.

(23) Dou, T.; Lian, T.; Shu, S.; He, Y.; Jiang, J. The substrate and inhibitor binding mechanism of polyspecific transporter OAT1 revealed by high-resolution cryo-EM. *Nat. Struct Mol. Biol.* **2023**, *30* (11), 1794−1805.

(24) Shan, Z.; Yang, X.; Liu, H.; Yuan, Y.; Xiao, Y.; Nan, J.; Zhang, W.; Song, W.; Wang, J.; Wei, F.; et al. Cryo-EM structures of human organic anion transporting polypeptide OATP1B1. *Cell Res.* **2023**, *33* (12), 940−951.

(25) Parker, J. L.; Kato, T.; Kuteyi, G.; Sitsel, O.; Newstead, S. Molecular basis for selective uptake and elimination of organic anions in the kidney by OAT1. *Nat. Struct Mol. Biol.* **2023**, *30* (11), 1786−1793.

(26) Ciuta, A. D.; Nosol, K.; Kowal, J.; Mukherjee, S.; Ramirez, A. S.; Stieger, B.; Kossiakoff, A. A.; Locher, K. P. Structure of human drug transporters OATP1B1 and OATP1B3. *Nat. Commun.* **2023**, *14* (1), 5774.

(27) Zeng, Y. C.; Sobti, M.; Quinn, A.; Smith, N. J.; Brown, S. H. J.; Vandenberg, J. I.; Ryan, R. M.; O'Mara, M. L.; Stewart, A. G. Structural basis of promiscuous substrate transport by Organic Cation Transporter 1. *Nat. Commun.* **2023**, *14* (1), 6374.

(28) Suo, Y.; Wright, N. J.; Guterres, H.; Fedor, J. G.; Butay, K. J.; Borgnia, M. J.; Im, W.; Lee, S. Y. Molecular basis of polyspecific drug and xenobiotic recognition by OCT1 and OCT2. *Nat. Struct Mol. Biol.* **2023**, *30* (7), 1001−1011.

(29) Khanppnavar, B.; Maier, J.; Herborg, F.; Gradisch, R.; Lazzarin, E.; Luethi, D.; Yang, J. W.; Qi, C.; Holy, M.; Jantsch, K.; et al. Structural basis of organic cation transporter-3 inhibition. *Nat. Commun.* **2022**, *13* (1), 6714.

(30) Zhang, S.; Zhu, A.; Kong, F.; Chen, J.; Lan, B.; He, G.; Gao, K.; Cheng, L.; Sun, X.; Yan, C.; et al. Structural insights into human organic cation transporter 1 transport and inhibition. *Cell Discov* **2024**, *10* (1), 30.

(31) Drew, D.; North, R. A.; Nagarathinam, K.; Tanabe, M. Structures and General Transport Mechanisms by the Major Facilitator Superfamily (MFS). *Chem. Rev.* **2021**, *121* (9), 5289−5335.

(32) Jiang, D.; Zhao, Y.; Wang, X.; Fan, J.; Heng, J.; Liu, X.; Feng, W.; Kang, X.; Huang, B.; Liu, J.; et al. Structure of the YajR transporter suggests a transport mechanism based on the conserved motif A. *Proc. Natl. Acad. Sci. U. S. A.* **2013**, *110* (36), 14664−14669.

(33) He, J.; Liu, G.; Kong, F.; Tan, Q.; Wang, Z.; Yang, M.; He, Y.; Jia, X.; Yan, C.; Wang, C.; et al. Structural basis for the transport and substrate selection of human urate transporter 1. *Cell Rep* **2024**, *43* (8), No. 114628.

(34) Dai, Y.; Lee, C. H. Transport mechanism and structural pharmacology of human urate transporter URAT1. *Cell Res.* **2024**, *34* (11), 776−787.

(35) Suo, Y.; Fedor, J. G.; Zhang, H.; Tsolova, K.; Shi, X.; Sharma, K.; Kumari, S.; Borgnia, M.; Zhan, P.; Im, W.; Lee, S. Y. et al.Molecular basis of the urate transporter URAT1 inhibition by gout drugs. *bioRxiv* **2024**. DOI: .

(36) Guo, W.; Wei, M.; Li, Y.; Xu, J.; Zang, J.; Chen, Y.; Chen, L. Mechanisms of urate transport and uricosuric drugs inhibition in human URAT1. *bioRxiv* **2024**, 2024.2009.2008.611941. DOI: .

(37) Wu, C.; Zhang, C.; Jin, S.; Wang, J. J.; Dai, A.; Xu, J.; Zhang, H.; Yang, X.; He, X.; Yuan, Q.; Hu, W.; Xu, Y.; Wang, M.; Jiang, Y.; Yang, D.; Xu, H. E. et al.Molecular mechanisms of uric acid transport by the native human URAT1 and its inhibition by anti-gout drugs. *bioRxiv* **2024**, 2024.2009.2011.612394. DOI: .

(38) Zhao, Z.; Jiang, Y.; Li, L.; Chen, Y.; Li, Y.; Lan, Q.; Wu, T.; Lin, C.; Cao, Y.; Nandakumar, K. S.; et al. Structural Insights into the Atomistic Mechanisms of Uric Acid Recognition and Translocation of Human Urate Anion Transporter 1. *ACS Omega* **2020**, *5* (51), 33421−33432.

(39) Sato, M.; Wakayama, T.; Mamada, H.; Shirasaka, Y.; Nakanishi, T.; Tamai, I. Identification and functional characterization of uric acid transporter Urat1 (Slc22a12) in rats. *Biochim. Biophys. Acta* **2011**, *1808* (6), 1441−1447.

(40) Tan, P. K.; Ostertag, T. M.; Miner, J. N. Mechanism of high affinity inhibition of the human urate transporter URAT1. *Sci. Rep* **2016**, *6*, 34995.

(41) Wu, D.; Chen, Q.; Yu, Z.; Huang, B.; Zhao, J.; Wang, Y.; Su, J.; Zhou, F.; Yan, R.; Li, N.; et al. Transport and inhibition mechanisms of human VMAT2. *Nature* **2024**, *626* (7998), 427−434.

(42) Dalton, M. P.; Cheng, M. H.; Bahar, I.; Coleman, J. A. Structural mechanisms for VMAT2 inhibition by tetrabenazine. *Elife* **2024**, *12*, RP91973.

(43) Jumper, J.; Evans, R.; Pritzel, A.; Green, T.; Figurnov, M.; Ronneberger, O.; Tunyasuvunakool, K.; Bates, R.; Zidek, A.; Potapenko, A.; et al. Highly accurate protein structure prediction with AlphaFold. *Nature* **2021**, *596* (7873), 583−589.

(44) Bai, X.; Moraes, T. F.; Reithmeier, R. A. F. Structural biology of solute carrier (SLC) membrane transport proteins. *Mol. Membr. Biol.* **2017**, *34* (1−2), 1−32.

(45) Zhang, X. C.; Zhao, Y.; Heng, J.; Jiang, D. Energy coupling mechanisms of MFS transporters. *Protein Sci.* **2015**, *24* (10), 1560−1579.

(46) Azevedo, V. F.; Kos, I. A.; Vargas-Santos, A. B.; da Rocha Castelar Pinheiro, G.; Dos Santos Paiva, E. Benzbromarone in the treatment of gout. *Adv. Rheumatol* **2019**, *59* (1), 37.

(47) Choi, H. K.; Mount, D. B.; Reginato, A. M. Pathogenesis of gout. *Ann. Intern. Med.* **2005**, *143* (7), 499−516.

(48) Leask, M. P.; Crisan, T. O.; Ji, A.; Matsuo, H.; Kottgen, A.; Merriman, T. R. The pathogenesis of gout: molecular insights from genetic, epigenomic and transcriptomic studies. *Nat. Rev. Rheumatol* **2024**, *20* (8), 510−523.

(49) Kaufmann, D.; Chaiyakunapruk, N.; Schlesinger, N. Optimizing Gout Treatment: A Comprehensive Review of Current and Emerging Uricosurics. *Joint Bone Spine* **2025**, *92*, No. 105826.

(50) Sun, C.; Zhang, M.; Zhao, Y.; Pang, J.; Peng, Y.; Zheng, J. An LC-MS/MS- and hURAT1 cell-based approach for screening of uricosuric agents. *J. Chromatogr B Analyt Technol. Biomed Life Sci.* **2020**, *1159*, No. 122336.

(51) Punjani, A.; Rubinstein, J. L.; Fleet, D. J.; Brubaker, M. A. cryoSPARC: algorithms for rapid unsupervised cryo-EM structure determination. *Nat. Methods* **2017**, *14* (3), 290−296.

(52) Pettersen, E. F.; Goddard, T. D.; Huang, C. C.; Couch, G. S.; Greenblatt, D. M.; Meng, E. C.; Ferrin, T. E. UCSF Chimera–a visualization system for exploratory research and analysis. *J. Comput. Chem.* **2004**, *25* (13), 1605−1612.

(53) Emsley, P.; Cowtan, K. Coot: model-building tools for molecular graphics. *Acta Crystallogr., Sect. D: Biol. Crystallogr.* **2004**, *60* (Pt 12 Pt 1), 2126−2132.

(54) Afonine, P. V.; Poon, B. K.; Read, R. J.; Sobolev, O. V.; Terwilliger, T. C.; Urzhumtsev, A.; Adams, P. D. Real-space refinement in PHENIX for cryo-EM and crystallography. *Acta Crystallogr., Sect. D: Struct. Biol.* **2018**, *74* (Pt 6), 531−544.

(55) Pettersen, E. F.; Goddard, T. D.; Huang, C. C.; Meng, E. C.; Couch, G. S.; Croll, T. I.; Morris, J. H.; Ferrin, T. E. UCSF ChimeraX: Structure visualization for researchers, educators, and developers. *Protein Sci.* **2021**, *30* (1), 70−82.

(56) Jo, S.; Kim, T.; Iyer, V. G.; Im, W. CHARMM-GUI: A web-based graphical user interface for CHARMM. *J. Comput. Chem.* **2008**, *29* (11), 1859−1865.

(57) Case, D. A.; Aktulga, H. M.; Belfon, K.; Cerutti, D. S.; Cisneros, G. A.; Cruzeiro, V. W. D.; Forouzesh, N.; Giese, T. J.; Götz, A. W.; Gohlke, H.; et al. AmberTools. *J. Chem. Inf. Model.* **2023**, *63* (20), 6183−6191.

(58) Humphrey, W.; Dalke, A.; Schulten, K. VMD: visual molecular dynamics. *J. Mol. Graph* **1996**, *14* (1), 33−38.